Chemistry Africa
https://doi.org/10.1007/s42250-022-00398-1

ORIGINAL ARTICLE

Tin Modified Fe_2O_3 Thick Films for Monitoring Environmental and Industrial Pollutant Gases

Vikas V. Deshmane[1] · Sarika Shinde[2] · Dharma K. Halwar[3] · Gotan Jain[2] · Arun V. Patil[4]

Received: 29 April 2022 / Accepted: 6 June 2022

Abstract

Main purpose of the current work was to study the effect of tin (Sn) addition on the synthesized iron oxide (Fe_2O_3). The catalytic nature of tin (Sn) can alter the structural, electrical and gas sensing properties of Fe_2O_3. The hazardous and pollutant gases can be sensed using Sn added Fe_2O_3 films. The Fe_2O_3 nanoparticles were synthesized using the co-precipitation method. 1, 3, 5, and 7 wt. % tin was added in iron oxide. The structural parameters of prepared gas sensor films were analyzed using X-Ray diffraction (XRD) analysis, scanning electron microscopy (SEM), and Energy Dispersive X-Ray Analysis (EDX). Williamson Hall plots were used to find out the microstructural parameters of the prepared films. The crystallite size was revealed to be below 10 nm. SEM micrograph revealed agglomerated, spherical, and granular nature with voids. The specific surface area was found to augment with an increase in tin doping. EDX exploration showed that films were non-stoichiometric i.e. oxygen deficient. The gas-sensing performance of the tin-modified Fe_2O_3 films was tested against pollutant gases like ethanol, ammonia LPG, NO_2, and petrol vapors. Excellent relative response and selectivity was recorded in presence of LPG. The Sn added Fe2O3 films performed as an effective LPG gas sensor.

Graphical Abstract

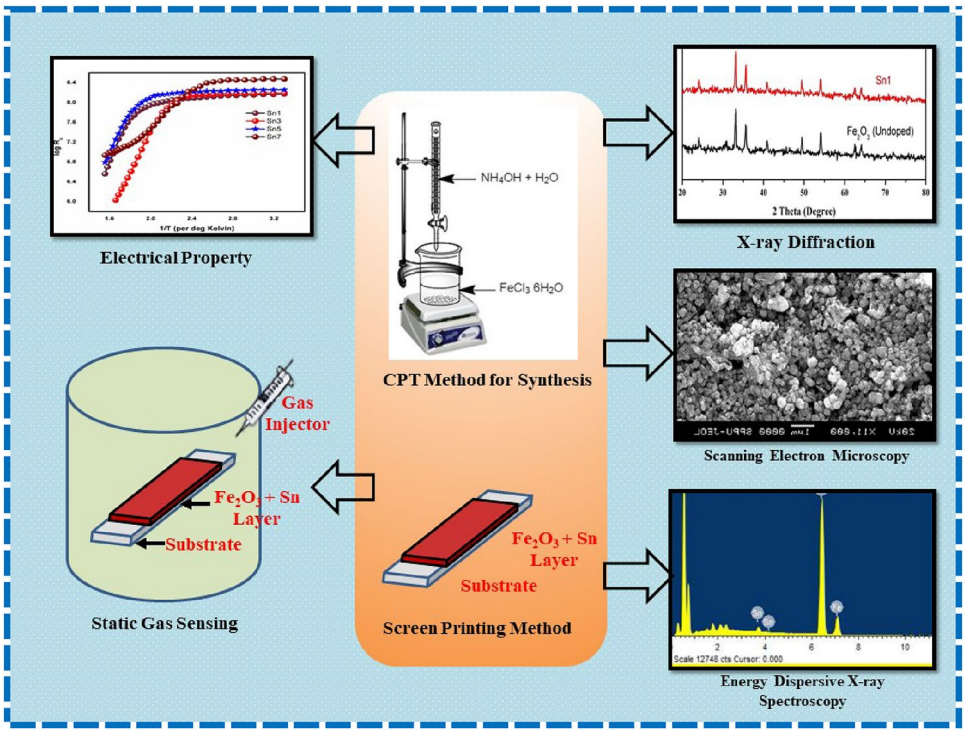

Extended author information available on the last page of the article

Published online: 30 June 2022

Keywords Hematite · Tin · XRD · SEM · EDX · LPG

1 Introduction

With the increase in industrialization, the exposure against the pollutant and hazardous gases is frequent for the human beings. The global warming is also becoming the key challenge in front of humanity. The exposure to hazardous gases can severely deuterate the health, and hence the efficient gas sensor options needs to be explored.

Chemo-resistive sensors have played a vital role in transducer research. Any kind of change in chemical properties can be quantified using variation in the resistance of the sample [1]. Metal oxide semiconductors (MOS) have been studied for their various application in sensor technology [2]. Modification of MOS properties can be achieved using various additives and dopants.

Thick films are robust hence can provide stable response over a time. Some of the investigations have utilized SnO_2 thick films for gas sensing applications [3] (Journal of applied Physics). The Iron oxide [4] (baularia 2013) and gold modified iron oxide films (baularia 2015) [5] were used for gas sensing investigations. A Mirzaei et al. have also extensively reviewed the hematite based gas sensors [6].

The current study used iron oxide as the base material as it is easily available, cheaper, low toxic, and stable against any environmental changes [7]. Iron oxide has various phases like α, β, γ, δ and ε. The alpha phase of iron oxide is the most stable. Other phases get transformed over a longer temperature range [8, 9]. These phases change due to surroundings and aging. It would be better to use stable base material and modify its properties using proper dopant. Properties like electron–hole recombination rate, hole diffusion length, and speed of charge transfer can be modified using various dopants/additives.

The co-precipitation method was used for the synthesis of iron oxide as it is cost-effective and easy to reproduce. The synthesized nano-sized hematite particles (α-Fe_2O_3) were of nano-scale. In most of the studies for gas sensing applications, iron oxide has been used as a dopant. Various dopants like platinum [10], molybdenum and chromium [11], gallium [12], sulphur [13], palladium [14], titanium, and magnesium [15], gold [16], and silver [17] have been used to modify properties of iron oxide. Very few studies have used the alpha phase of iron oxide as the base metal oxide material for gas detection.

The catalytic properties of metals have been employed to modify the electronic behavior of iron oxide. Tin is a column IV element. It has oxidation states of + 4 and + 2. Out of these states, the + 4 state is more stable than the + 2 state of tin. It has a melting point of 231.9 °C. It is fairly easy to convert tin (II) compounds to tin (IV) compounds. Tin (II) ions also reduce iron (III) ions to iron (II) ions. Tin oxide is amphoteric i.e. it shows both basic and acidic properties. Here tin is used as an additive to create defects in stable alpha iron oxide, which in turn will increase the response of the films to various gases.

In current work, qualitative and quantitative effects of the addition of tin (Sn) (1, 3, 5, and 7 wt. %) on morphological, structural, elemental variations of hematite (α-Fe_2O_3) films have been studied. Screen printed films were exposed against ethanol vapors, ammonia (NH_4), nitrogen dioxide (NO_2), liquefied petroleum gas (LPG), and petrol vapors at various concentrations like 200, 400, 600, 800, and 1000 ppm. The observations indicated the Sn added Fe_2O_3 films performed as efficient LPG sensor.

2 Materials and Methods

The AR grade chemicals were used in the present research work for the fabrication of undoped and tin-doped Fe_2O_3 nanoparticles. The chemicals used in the present research were used without any further process.

2.1 Synthesis of Undoped and Tin Modified Nanoparticles and Gas Sensor Films

The co-precipitation method was reported as one of the simple methods to synthesize iron oxide nanoparticles [18]. The cost effectiveness and easier reproducibility are some key advantages of this method. An NH_4OH and H_2O solution was prepared in the ratio of 1:1. The iron salt i.e. $FeCl_3$ $6H_2O$ (10 gm) was dissolved in double-distilled water (100 mL) at room temperature (29 °C) with continuous stirring. NH_4OH and H_2O solution was added dropwise in an aqueous solution of $FeCl_3$ $6H_2O$. The dispersion was stirred for 1 h and then heated at 80 °C for 2 h. The obtained precipitate was filtered, washed several times using de-ionized water, and dried to furnish brown color powder. The prepared powder was calcined at 500 °C for 4 h in a muffle furnace to give brown color iron oxide nanoparticles. The gas sensor films were formulated using the prepared iron oxide nanoparticles.

The inorganic and organic materials were used in 70:30 wt. proportion. Inorganic material consists of the base material i.e. synthesized iron oxide (α-Fe_2O_3 / Hematite) and tin (Sn) weight percentage (1, 3, 5, and 7% of inorganic material) of the films. Organic material contains 92% butyl Carbitol acetate (BCA) which plays the role of a vehicle

to prepare paste and 8% ethyl cellulose which acts like temporary binder. The iron oxide, tin, and ethyl cellulose were mechanically mixed and ground using mortar pestle for about 10 min. Temporary binder ethyl cellulose binds all materials with each other as well as with the substrate. BCA was added drop-wise to maintain the proper thixotropic properties of the paste [19]. The paste was applied using the screen printing method over 1 cm × 2.5 cm area of the glass substrate. After the time for settlement, the films were dried under infrared radiation for 45 min and fired at temperatures of 450 °C for 1.5 to 2 h in a muffle furnace. The films were found to be well adhering to the glass substrate which was very necessary for further characterization.

The authors used relative density formula to calculate the thickness of the film. The designed area of the material on the glass substrate was 1.25 cm × 2.5 cm. The mass of film before and after photo-lithography was used to measure the mass of the material present on the substrate. The only thickness of the films was calculated using the formula for density i.e.

Film Thick ness = (Density * Length * Breadth) / Mass of the material. The thickness of the film was about 20 µm.

2.2 Analysis of Structural, Electrical, and Gas Sensing Properties

The structure of the films was confirmed using X-ray diffraction study (XRD).

The morphological analysis was completed using scanning electron microscopy (SEM) [Model JOEL 6300(LA) Germany]. The elemental constituents were measured by energy dispersive x-ray analysis (EDX). The electrical and gas sensing properties were analyzed in static gas sensing apparatus at the research center.

The static gas sensing analysis was performed inside a 20 l glass chamber in air atmosphere (Fig. 1). The ammonia (NH_4, using liquid ammonia), and nitrogen dioxide (NO_2, using copper fillings and nitric acid) were prepared in laboratories and injected inside chamber at various temperature and concentrations. The vapors of ethanol, petrol and LPG were also utilized as target gases. The target gases were selected considering the daily exposure to these common pollutants. The NO_2 (exposed from vehicles), LPG (household leakage), NH_3 (decomposed waste matter, public lavatory), petrol vapors (at the petrol pumps) and ethanol vapors (fermented agricultural products / beverages) were investigated in current research work.

The 20 ml gas inserted in 20 l glass container would be the 1000 ppm concentration of that gas. Likewise other concentrations of target gas (200, 400, 600, 800, and 1000 ppm) were injected inside the chamber using an injector. The output voltage was recorded on micro voltmeter and used for further analysis. The change in resistance of the films in air and in presence of target gas was used to calculate the relative response of the films. The response time is the time taken for increase in relative response from zero to the 90% of the maximum value. The recovery time is the time taken to recover 90% of the original resistivity. These gas sensing parameters were analyzed and reported.

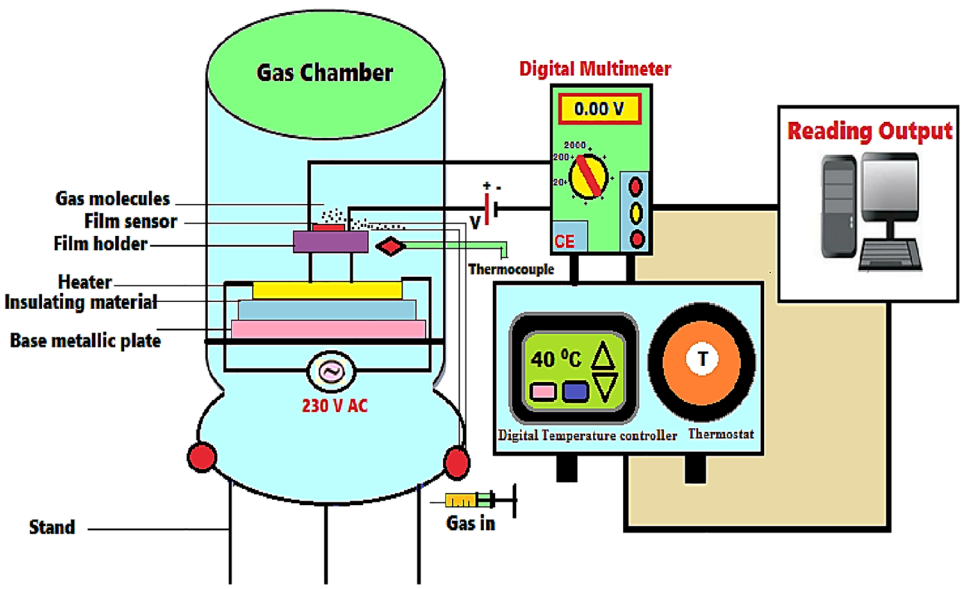

Fig. 1 Block diagram for static gas sensing setup used in present research

3 Results and Discussion

3.1 Structural Analysis

XRD was employed to find out the content and structure of the films. The average crystallite size was calculated from the XRD pattern using the following Debye Scherer's formula [20]. This formula used the full angular width of a diffraction peak at the half maxima peak intensity (β), a wavelength of X-radiation (λ).

$$D = \frac{0.9\,\lambda}{\beta\,\cos\theta} \tag{1}$$

Figure 2 shows the XRD plot for the 1%, 3%, 5%, 7% Sn added films, termed as Sn1, Sn3, Sn5, and Sn7 respectively. As per JCPDS #86–0550 data, the major content of the films is Hematite (α-Fe_2O_3). The JCPDS #22–0336 data also supports the presence of tin (Sn). The major peaks were at 24.103, 33.138, 35.711, 40.859, 49.420, 54.00, 62.50 and 64.07 position which correspond to [012], [104], [110], [113], [024], [116], [214], and [300] planes. Most favored plane was observed to be along [104] direction. Some of the peaks for tin (Sn) were not observed due to less amount of tin. The low intensity of peaks for tin might be due to the very low amount of tin present in the films. Crystallite size was calculated using the Scherer formula (Eq. 1). The XRD plot supports the crystalline nature of the content of the films.

Figure 3a–d is the Williamson Hall plots (W–H plot) for 1, 3, 5, and wt. 7% Sn added hematite films. The intercepts and slopes of corresponding films are tabulated in Table 1.

W–H plot is representative of Eq. 2. The equation involves variables like full width at half maximum (β), effective crystalline size (ε), effective strain (η), the wavelength of the sources (λ), and position of the peak (θ) [21].

$$\frac{\beta\cos\theta}{\lambda} = \frac{1}{s} + \frac{n\sin\theta}{\lambda} \tag{2}$$

W–H plot is used to find out the microstructural parameters of the films. W/H plot intercepts are gradually increasing, which indicates the increment in particle size. At the same time slope of the W–H plotline is also increasing indicating an increase in longitudinal strain. Longitudinal strain causes a change in size which is reflected in the crystallite size calculated from the Scherer formula. Table 1 also indicates that as additive percentage increases longitudinal strain increases which causes an increase in crystallite size [22].

3.2 Scanning Electron Microscope (SEM) Analysis and Energy-Dispersive X-ray Spectroscopy (EDX) Analysis

Morphology of the prepared films of 1, 3, 5, and 7 wt. % Sn additive were analyzed using SEM analysis [Model JOEL 6300(LA) Germany]. The specific surface area of thick films was calculated from SEM using the BET method for

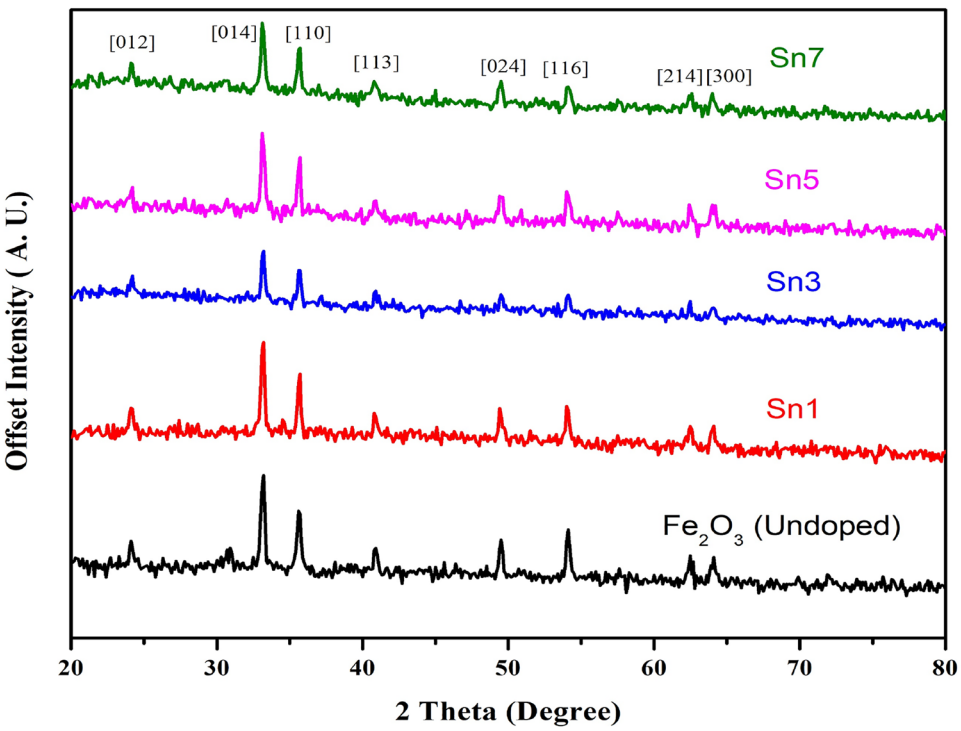

Fig. 2 XRD stack of 1, 3, 5, 7 wt. % Sn added hematite films

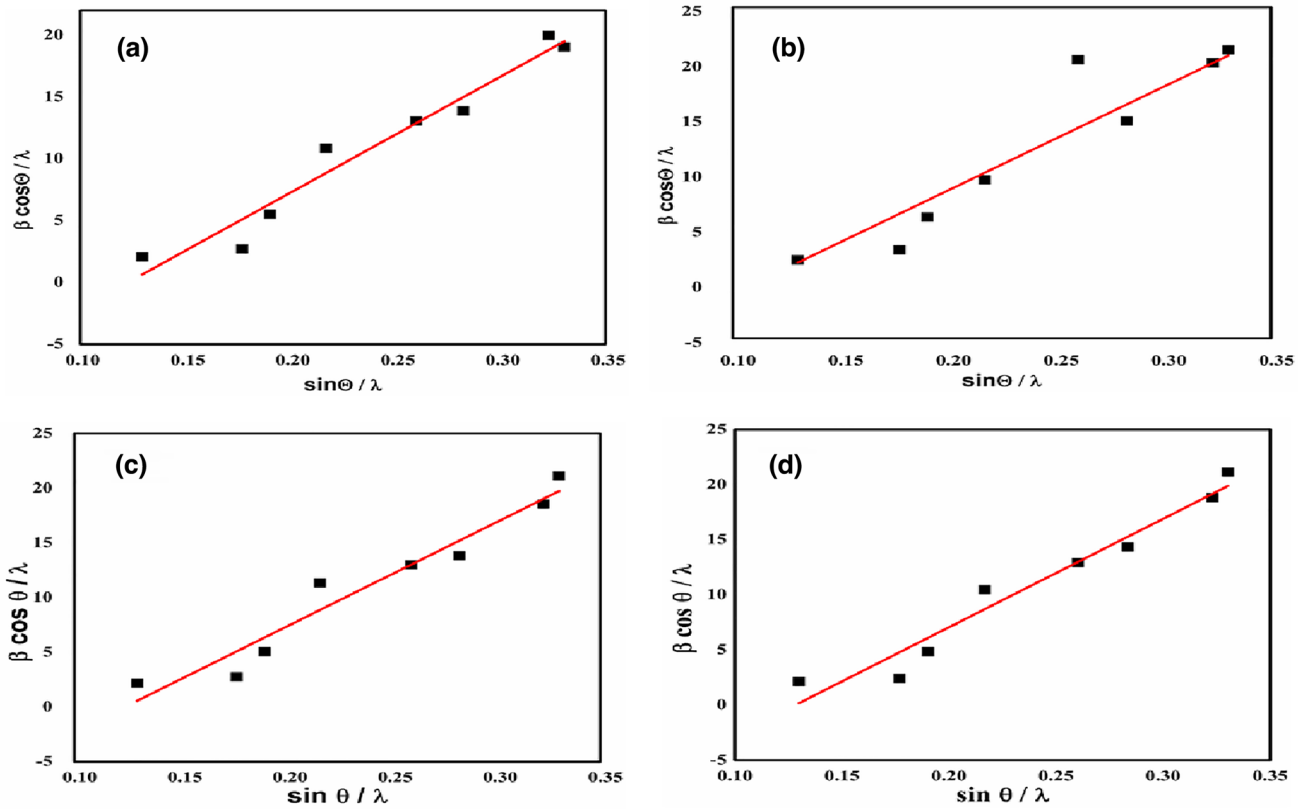

Fig. 3 W–H plot for (**a**) 1 (**b**) 3 (**c**) 5 and (**d**) 7 wt. % Sn added iron oxide films

Table 1 Crystallite size, specific surface area, WH plot parameters of 1, 3, 5, and 7 wt. % tin added iron oxide films

Property	1% Sn	3% Sn	5% Sn	7% Sn
Crystallite size from XRD plot (nm)	3.34	2.99	3.28	3.71
W–H plot intercept	− 11.517	− 10.354	− 11.841	− 12.599
W–H plot slope	93.831	93.831	95.553	98.329
Specific surface area (From SEM) ($m.^2$/gm)	6.372	7.056	7.117	7.272

spherical particles using Eq. 3. Here d is the diameter of the particle and ρ is the composite density of the materials.

$$S_w = 6 / \rho d \tag{3}$$

Figure 4a–d shows the SEM images for 1, 3, 5, and wt. 7% Sn added Hematite films respectively which showed agglomerations. The shape of particles appeared to be nearly spherical with clear voids in between the granules. The islands Sn were seen which indicated the non-homogeneous distribution of the additive. Table 1 contains specific surface area, calculated using formula 3. As the particle size decreased the specific surface area of the particle increased.

As seen in the Fig. 3a–d, as the weight percentage of tin increases the agglomeration appears to be diminishing. The presence of extra tin could have hampered the agglomerating nature of base material.

SEM micrographs show particle agglomerations which may be due calcination process. The melting point of tin is 231.9 °C, while films were calcined at 450 °C. The tin atoms got separated during molten state and after air cooling, it might have agglomerated on neighboring atoms. Nearly isotropic agglomeration might have caused almost spherical particles observed in the micrograph. This spherical nature augmented surface to volume ratio, which improved the amount of target gas or atmospheric oxygen adsorption. Clear voids were seen in-between particles. Voids can be attributed to the defects created by the additive, desorption of oxygen from the base material of iron oxide, and agglomerating nature of the material. Due to the increase in additive percentage the relative density of the material decreased which caused an increase in specific surface area. More is the specific surface area more will be the rate of adsorption of the target gas. The surface to volume ratio, particle

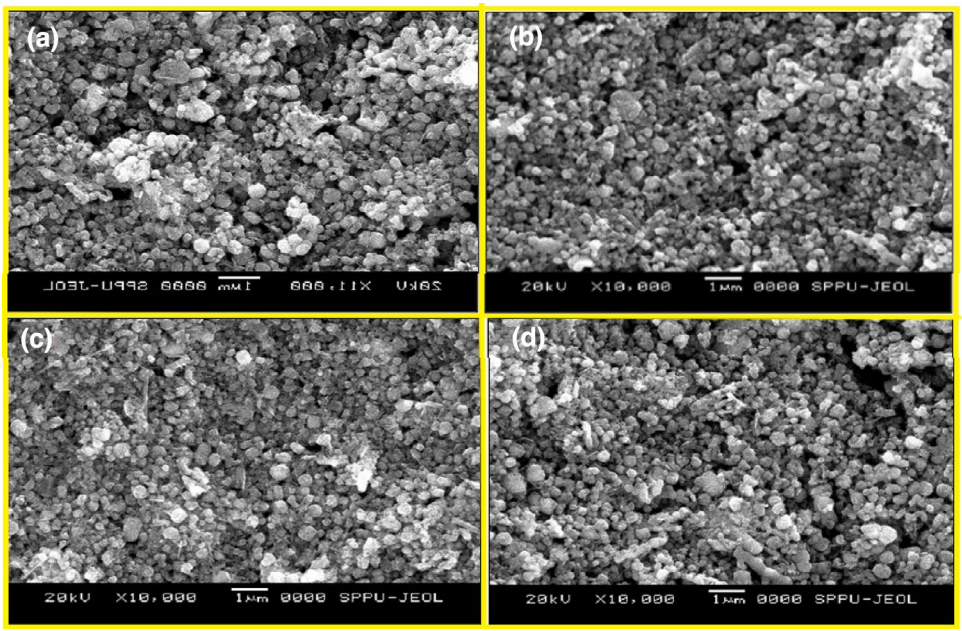

Fig. 4 SEM micrographs for (**a**) 1 (**b**) 3 (**c**) 5 and (**d**) 7 wt. % Sn added Hematite films

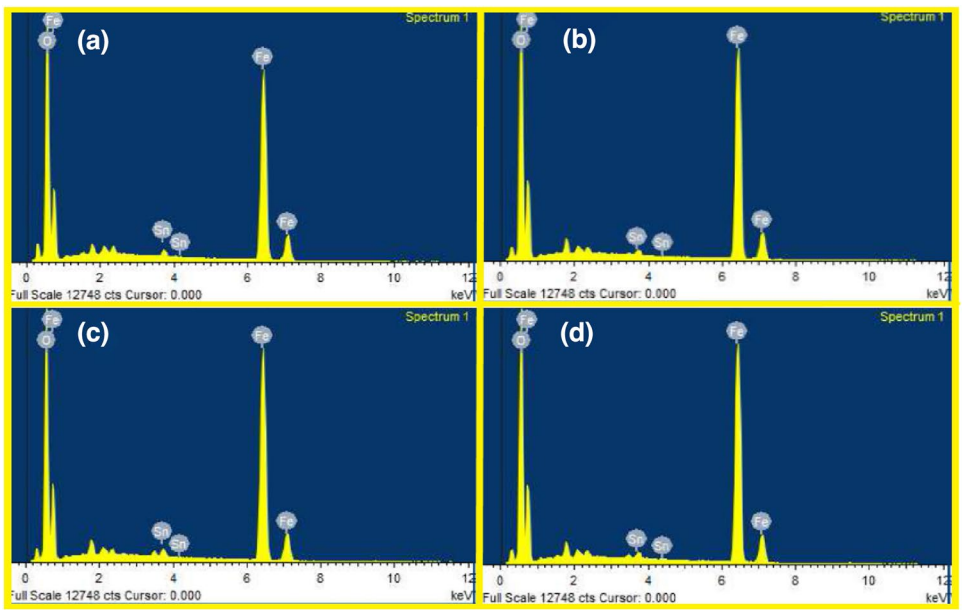

Fig. 5 EDS spectra for (**a**) 1 (**b**) 3 (**c**) 5 and (**d**) 7 wt. % Sn added iron oxide films

sphericity, and voids are the factors that enhance the gas sensing properties of the films.

Figure 5a–d shows EDX spectra of 1, 3, 5, and wt. 7% Sn added Hematite films. Energy dispersive spectra again supported the presence of Iron, Oxygen, and Indium. Certain minor peaks may be attributed to the presence of certain impurities [18]. In the current study, authors have used weight % method for base material and additives. The molecular weight of tin is 118.71 u which is higher as compared to that of iron (55.845 u), hence 7 wt. % of base material also showcased weak contribution to Sn in EDS spectra.

The elemental content was again confirmed using EDX analysis. Iron atomic % and weight % increased with additive percentage. The iron atomic percentage increased from 19.67 to 20.67. Oxygen atomic % decreased from 80.20 for 1% Sn added films to 79.07 for 7% Sn added films. Oxygen weight % was also found to decrease as per the additive

percentage. Tin atomic % increased from 0.13 to 0.31 as the additive % increased, while weight % also increase from 1.42 to 3.68. The films are found to be relatively oxygen deficient.

An increase in tin percentage is obvious since it was added externally. The oxygen depletion is causing the decrease in oxygen percentage [23]. The atomic percentage of iron was increasing while oxygen content was found to be decreasing. This oxygen deficiency caused an increase in gas relative response of 7% in added iron oxide films. Films were found to have elements in non-stoichiometric proportion and oxygen-deficient as per table II. A decrease in oxygen percentage creates interstitial vacancies i.e. defects that further affect gas sensing properties [19]. 7% Sn additive films were found to be relatively oxygen-deficient as compared to other films. These films would be more suitable for oxygen adsorption and hence gas sensing [18].

3.3 Analysis of Electrical Behaviour of Undoped and Modified Fe_2O_3 Thick Film Sensors

Figure 1 represents the static gas sensing appratus block diagram used in the present research. The resistivity of thick films at constant temperature is calculated using the below equation,

$$\rho = \frac{R \times b \times t}{l} \Omega.m^{-1} \tag{4}$$

In équation (4), the resistance of the thick film sample at constant temperature (*R), the* thickness of the thick film sample (*t),* length of the thick film sample (*l),* and breadth of the thick film sample (*b)* was used.

The temperature coefficient of resistance (TCR) of thick films fired at 500 °C was calculated by using the following relation,

$$TCR = \frac{1}{R_0}\frac{\Delta R_0}{\Delta T} K^{-1} \tag{5}$$

The activation energy of Sn added Fe_2O_3 films were calculated from the Arrhenius plot for low and high-temperature regions. This variation in resistance is reversible in both heating and cooling cycles obeying the Arrhenius equation [24]. Here the variables are resistance at constant temperature (R_o), the activation energy of the electron transport in the conduction band (ΔE), Boltzmann constant (K), and absolute temperature (T).

$$R = R_o e^{-\Delta E / KT} \tag{6}$$

Figure 6a shows the variation in resistance of 1, 3, 5, and wt. 7% Sn added Hematite films at varying temperatures. As the additive wt. % increased, the resistivity of of the films also amplified. The resistance of films decreased quickly for the films with higher tin wt. %

Figure 6a shows the variation in resistance of 1, 3, 5, and wt. 7% Sn added Hematite films at varying temperatures. As

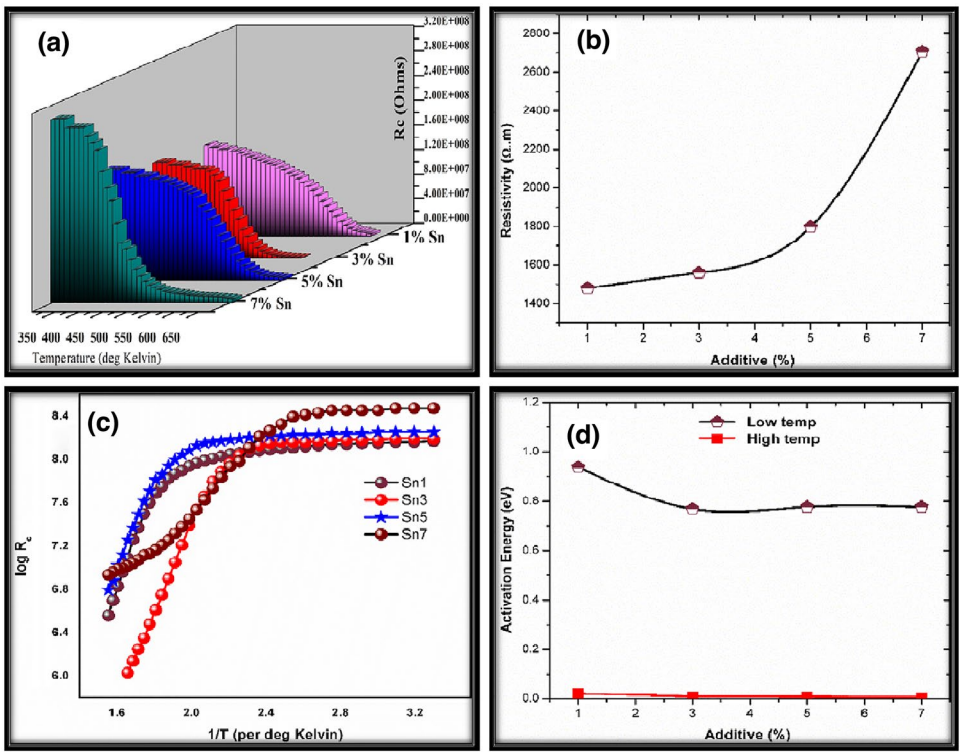

Fig. 6 (**a**) Resistance vs Temperature, (**b**) Resistivity variation, (**c**) log R_c vs 1/T, and (**d**) Activation energy variations for 1, 3, 5, and 7 wt. % Sn added Hematite films

Table 2 Electrical parameters for 1, 3, 5, and 7 wt. % Sn added Hematite films

Sample	Resistivity (Ωm)	TCR (per $^{O}K)10^{-3}$	Activation Energy (eV/.^{O}C)	
			High Temp. Region)	Low Temp Region
Sn1	1480	− 5.6869	0.9380	0.022500
Sn3	1560	− 11.1300	0.7690	0.009329
Sn5	1798	− 6.3712	0.7772	0.008628
Sn7	2707	− 8.7458	0.4215	0.006219

the additive wt. % increased, the resistivity of of the films also amplified. The resistance of films decreased quickly for the films with higher tin wt. %

The resistivity, TCR and activation energy 1, 3, 5, and wt. 7% Sn added Hematite films have been tabulated in Table 2.

As the wt. % of tin increased, the resistivity of the iron oxide films also incremented. Tin is reactive in the metal oxide environment because it has a low melting point of 231.9 °C. During the calcination, it may occupy the interstitial positions of Iron and hence generated defects in the Iron oxide structure. These defects increase as the number of tin increases, which in turn causes an increase in resistivity. As shown in Fig. 6b as tin wt. % increases resistance increases. This causes an increase in the slope of the graph. This is nothing but the increase in temperature coefficient of resistance.

Figure 6c shows a variation of log R_c versus 1000/T having two distinct regions. The first is the high-temperature region and the second is the low-temperature region. Each plot has a transition temperature separating it into two regions. The activation energy is the energy required by the thin films sample to transform from a highly resistant state to a low resistant state and vice versa. As tin additive percentage increases, it created more defects with the discontinuities in the film surface causing the increase in resistivity. Therefore activation energy for high temperature and low-temperature regions were found to decrease with an increase of additive weight percentage as per Fig. 6d.

3.4 Analysis of Static Gas Sensing Behaviour of Undoped and Modified Fe_2O_3 Thick Film Sensors

Gas sensing behavior was studied in a static gas sensing set up in the air atmosphere. The response (%) of film for any gas was calculated using Eq. 7. *Ra* was the resistance of thick film in the air atmosphere and *Rg* was resistance to thick film in the gaseous atmosphere [25].

$$Response\,(\%) = \left|(Ra - R_{g)}/R_a\right| * 100 \quad (7)$$

The selectivity of films for target gas was found out using the following Eq. 8. $S_{\text{other gas}}$ was the relative response of films for the gas other than target gas and $S_{\text{target gas}}$was relative response for films for the target gas (LPG).

$$Relative\,Response = \left(S_{other\,gas}/S_{target\,gas}\right) * 100 \quad (8)$$

The gas sensing properties of 1, 3, 5, and 7 wt. % of tin added Hematite samples were tested against ethanol vapors, ammonia, NO_2, LPG, and petrol vapors at 50, 100, 150, 200, 250, 300, 350, and 400 °C. All outputs were used to calculate relative response and selectivity. Figure 7a–d shows the variation of the relative response of 1, 3, 5, and 7 wt. % Sn added Hematite fi In Table 3, from sample at 1%Sn to 3%Sn, the atomic % decrease while wt% increase for various temperatures in presence of ammonia (NH_3), nitrogen dioxide (NO_2), ethanol, LPG, and Petrol vapors respectively. Figure 7e shows a comparative gas response of 1, 3, 5, and 7 wt. % Sn added Hematite films at 300 °C.

The 7% Sn added films showed good relative response (61%) against LPG at 300 °C as compared with other tested gases. 1% Sn added Fe_2O_3 films showed lowest relative response. 3% Sn added films displayed good relative response to petrol vapors at 250 °C. 5% Sn added iron oxide films showed a relative response (37%) to petrol vapors.

Figure 8a shows a variation of the relative response of 7% Sn added hematite films against LPG concentration. As the LPG concentration increases the relative response of the films also rises. An increase in LPG concentration creates more defects in films which improve adsorption, in turn, influences the relative response of the sample. Tin acts as a catalyst and lowers the activation energy. Due to the incorporation of tin, the iron oxide films transform from the high resistant stage to the low resistant stage. These factors influence molecular dissociation and the rate of the reaction.

The change in co-ordination geometry of the crystals is due to incorporation of the additive creates the defects. The crystalline defects escalate the surface to volume ratio and adsorption probability. More is oxygen species adsorbed, faster will be the oxidization of LPG. These factors impact the conductivity of the films in presence of LPG. The LPG sensing mechanism has been summarized in Fig. 9.

At higher temperatures, atmospheric oxygen adsorbs on the iron oxide film surface and extracts an electron from the conduction band of base material as,

$$O_2(air) + 2e^-(conduction\,band) \rightarrow 2O^-(film\,surface) \quad (9)$$

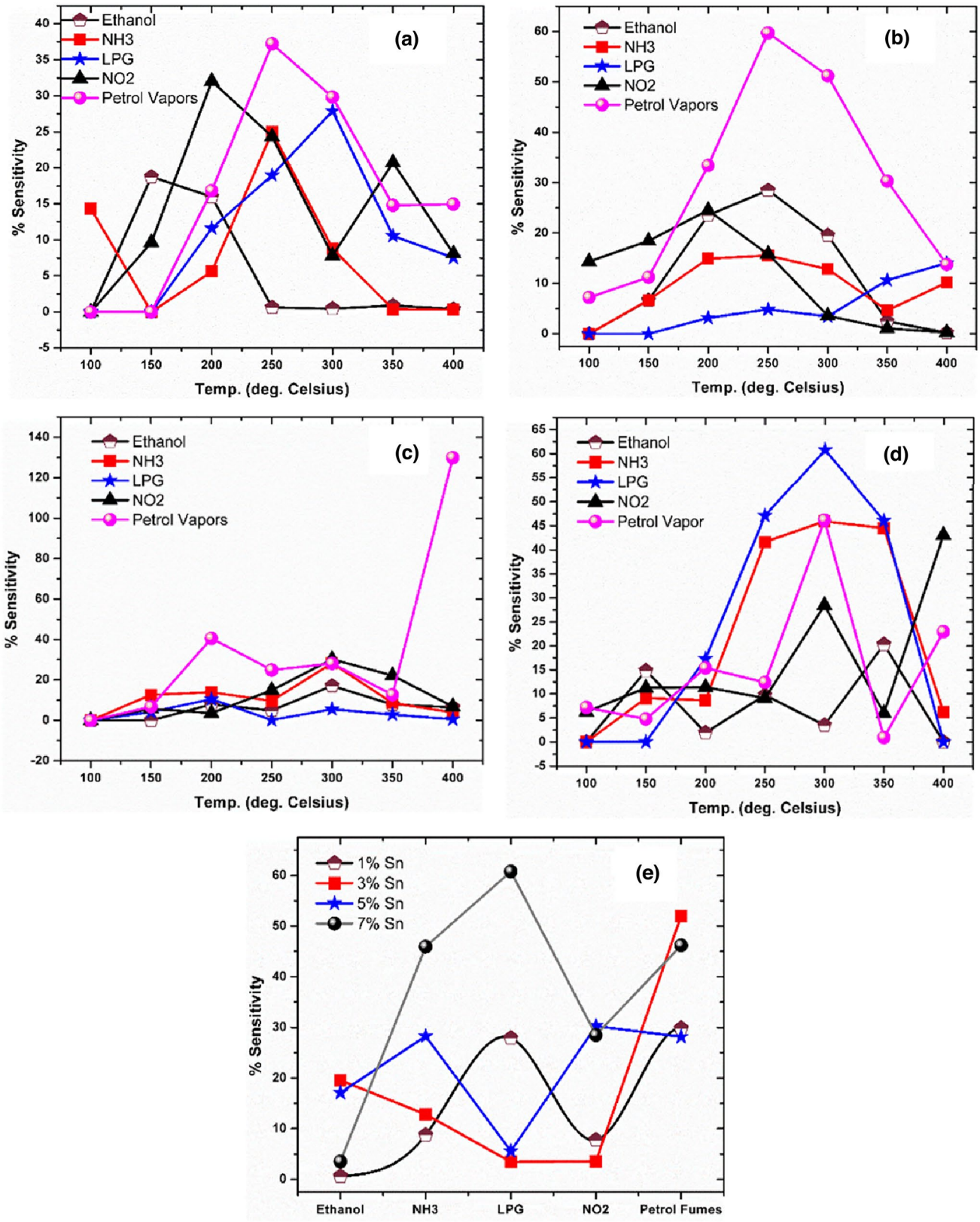

Fig. 7 (**a–d**) Gas response of 1, 3, 5, and 7 wt. % Sn added Hematite films (**e**) Gas response of 1, 3, 5, and 7 wt. % Sn added Hematite films at 300 °C

Table 3 Relative weight percentage and atomic percentage of iron, tin, and oxygen from EDX spectra for 1, 3, 5, and 7 wt. % Sn added Hematite films

Element	1% Sn		3% Sn		5% Sn		7% Sn	
	Atomic %	Wt %	Atomic %	Wt %	Atomic %	Wt %	Atomic %	Wt %
Fe	19.67	103.83	20.24	113.22	20.69	115.77	20.62	113.79
O	80.20	121.25	79.61	127.56	79.08	126.76	79.07	125.01
Sn	0.13	1.42	0.14	1.71	0.23	2.72	0.31	3.68

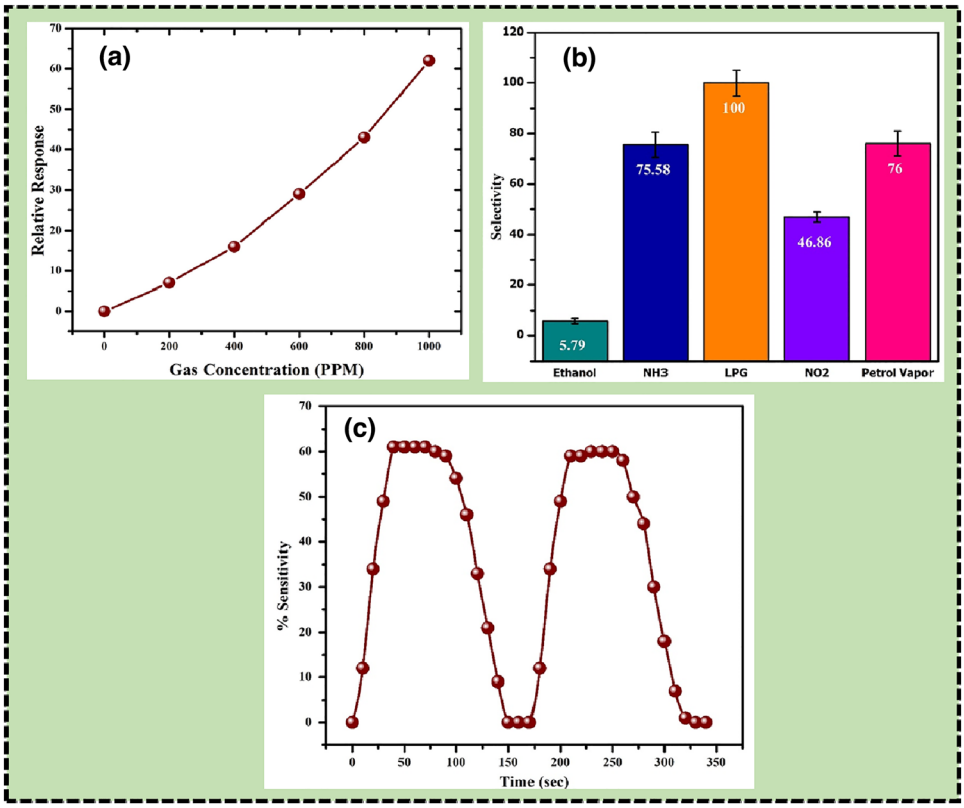

Fig. 8 (**a**) shows a variation of the relative response of 7% Sn added hematite films against LPG concentration. (**b**) Relative selectivity & (**c**) Relative response against time of 7% Sn added hematite films at 300 °C to LPG

The number of conduction electrons in iron oxide reduces, causing an increase in film resistance. When LPG reacts with surface oxygen, displacement of oxygen takes place by dehydration. LPG gets oxidized to CO_2 and H_2O by following a series having intermediate stages [26].

$$C_4H_{10}(gas) + 13O^{-}(film\ surface) \rightarrow 4CO_2(gas) + 5H_2O\,(gas) + 13e^{-} \quad (10)$$

The energy released in the decomposition of LPG molecules would be sufficient for trapped electrons to enter the conduction band of activated base material. The resistivity of the base material reduces. The higher wt. % of tin were escaped because if additive % increases further, the additive can mask the iron oxide (base material), resulting in diminishing response.

At an optimum temperature of 250 °C, 3% Sn added iron oxide films showed maximum relative response (60%) to petrol vapors. At a temperature of 300 °C, 7% tin added iron oxide films showed good relative response (63%) to LPG. At 300 °C, the films showed excellent selectivity against LPG compared to all other gases.

At lower temperatures films are not supplied with sufficient thermal energy therefore rate of reaction is slow and hence response is lower. The thermal energy required for the gas sensing mechanism is provided at the optimum temperature. At 300 °C exactly sufficient energy is provided to carry out the adsorption and desorption process with optimum reaction speed. However, the response decreases at higher operating temperature, as the oxygen adsorbates are desorbed from the surface of the sensor [27]. Thermal excitation at higher temperatures reduces

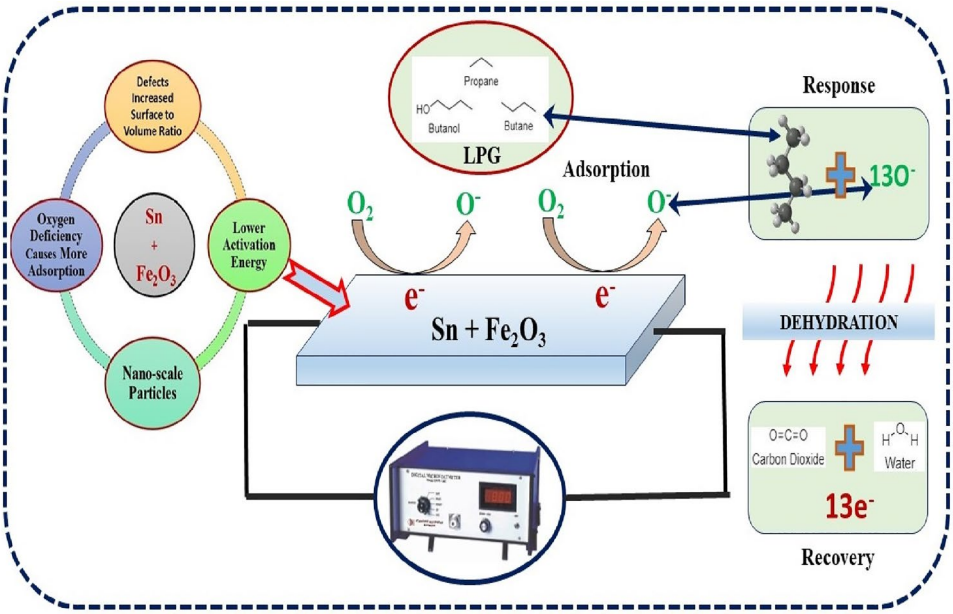

Fig. 9 LPG sensing mechanism based on dehydration

the path available for charge carriers i.e. Debye length. Therefore gas response at higher temperatures reduces [24].

Selectivity is defined as the ability of a sensor in responding to target gas in the presence of other gases. Percent selectivity of one gas over others is defined as the ratio of the maximum response of target gas (e.g. LPG) to the maximum response of other gas at an optimum temperature [28].

Figure 8b shows the comparative selectivity of 7% Sn added Fe_2O_3 films at 300 °C for various gases. At 250 °C, 3% Sn films are found to be more selective to petrol vapors compared to all other gases tested. While at 300 °C 7% Sn films also showed very good selectivity to petrol vapors as compared to ethanol, ammonia, LPG, and NO_2 gases but with relatively low selectivity.

The major constituent of LPG by volume is propane (carbon-3 aliphatic compound), and minor are propene and butanes [29]. Petrol vapors mainly contain aliphatic hydrocarbons with carbon number in decreasing order of quantity 4 n-Butane, 5 n-pentane, 6 n-hexane, 3 propane, and n-heptane and a negligible amount of aromatic hydrocarbons having a carbon number in decreasing order of quantity 6, 7, and 8. Above 4-carbon hydrocarbons, isomers are also present [30]. Ammonia, LPG, and Petrol vapor are the reducing gases. Selectivity of LPG may be attributed to the electron-donating ability of the gas/vapor [31].

Figure 8c shows the variation of the relative response of 7% Sn added Iron Oxide films at an optimum temperature of 300 °C to LPG versus time. Films showed a response time of about 37 s and recovery time of about 110 s. Recovery time was found to be comparatively high, due to the low speed of desorption. Maximum porosity and large surface-to-volume ratio increase response to the target gas. The response could be attributed to the adsorption–desorption type of sensing mechanism. Fast response time (37 s) should be due to the fast adsorption rate. Sluggish recovery time (110 s) should be due to the slow rate of desorption of target gas.

The outcomes of current study has been compared with the recent published work and summarized in Table 4. Very few of the recent research have used tin as an additive with the hematite as a base material.

Current study used relatively easier method of hematite synthesis i.e. co-precipitation method and film preparation i.e. photolithography. The synthesized particles have relatively lesser size (10 nm). Majority of hematite based gas sensors have reported good activity against ethanol but current study has maximum response against LPG. The response time (37 s) and recovery time (110 s) was also comparatively good.

However the films could be tested against lower concentration of LPG concentration in future. The reduction of optimum temperature (300 °C) for LPG sensing remains as the future scope of the study.

Table 4 Comparison of outcomes of current study with recent published work

Additive & base material	Synthesis method	Crystallite size (nm)	Optimum temp (deg Cel.)	Gas & concentration (ppm)	Response time (s) & recovery time (s)	Reference
Hematite	Sol–gel	60	225	NO_2 (10 ppm)	26 s & 48 s	[32]
Hematite	Solvo thermal	650	–	Acetone (100 ppm)	–	[33]
Hematite	Co-precipitation	40–60	171	LPG (1000 ppm)	96 s & 224 s	[34]
Silver (Ag) & Hematite	Co-precipitation & screen printing	76	Room Temp	Ethanol (2–35 mg $L.^{-1}$)	32 s & 27 s	[35]
Indium (In) & Hematite	Silica Template	23	300	Ethanol (100 ppm)	8 s & 1 s	[36]
Gold (Au) & Hematite	Electro-chemical anodization	70	350	Acetone (50 ppm)	3 s & 214 s	[37]
Palladium Oxide (PdO) & Hematite	Hydrothermal & Solution impregnation	–	–	H_2S (75 ppm)	–	[38]
Platinum (Pt) & Hematite	Hydrothermal synthesis and impregnation method	–	375	Dimethyl Disulphide (100 ppm)	1 s & 168 s	[39]
Reduced Graphene Oxide (rGO) & Hematite	Hydrothermal	20–30	400–450	Ethanol (100 ppm)	5 s	[40]
Tin (Sn) & Hematite	Co-precipitation	10	300	LPG (1000 ppm)	37 s & 110 s	Current study

4 Conclusion

Tin added hematite performed as an excellent LPG sensor. Nano-scale Iron oxide (Fe_2O_3) was prepared by the co-precipitation method. Films of tin additive and iron oxide were prepared using the screen printing method, which showed good adherence to the glass substrate. XRD supports the major presence of hematite (α-Fe_2O_3) and tin (Sn). An increase in additive % increases longitudinal strain that in turn increases the particle size. SEM and EDS analysis showed porous films of (α-Fe_2O_3) and tin (Sn) and higher was the additive % lower are the oxygen atomic percentage.7% tin added films showed 63% relative response to LPG at 300 °C. Response time was fast 37 s and recovery time was sluggish 110 s.

Acknowledgements The authors also would like to thank the Department of Chemistry and Department of Physics, MGV's Arts, Science and Commerce College, Manmad, Nashik, MS, India. The authors would also like to thank the Department of Physics, SICES Degree College, Ambarnath, Thane, MS, India and Thick and thin film laboratory, M.S.G. College, Malegaon, Nashik, Maharashtra, India

Funding This research did not receive any specific grant from funding agencies in the public, commercial, or not-for-profit sectors.

Declarations

Conflict of interest Authors declare no conflict of interest of any sort.

References

1. Miller D, Sheikh A, Morris P (2014) Nanoscale metal oxide-based heterojunctions for gas sensing: A review. Sens Actuators B Chem 204:250–272. https://doi.org/10.1016/j.snb.2014.07.074
2. Dey A (2018) Semiconductor metal oxide gas sensors: A review, Mater. Sci. Eng. B: Solid-State Mater. Adv. Technol. 229:206–217. https://doi.org/10.1016/j.mseb.2017.12.036
3. KhunKhun K, Mahajan A, Bedi R (2009) SnO2 thick films for room temperature gas sensing applications. J Appl Phys. https://doi.org/10.1063/1.3273323
4. Balouria V, Kumar A, Samanta S, Singh A, Debnath A, Mahajan A, Gupta S (2013) Nano-crystalline Fe_2O_3 thin films for ppm level detection of H_2S. Sens Actuators B: Chem 181:471–478. https://doi.org/10.1016/j.snb.2013.02.013
5. Balouria V, Ramgir N, Singh A, Debnath A, Mahajan A, Bedi R, Gupta S (2015) Enhanced H_2S sensing characteristics of Au modified Fe_2O_3 thin films. Sens Actuators B: Chem 219:125–132. https://doi.org/10.1016/j.snb.2015.04.113
6. Mirzaei A, Hashemi B, Janghorban K (2015) α-Fe_2O_3 based nanomaterials as gas sensors. J Mater Sci Mater Electron 27(4):3109–3144. https://doi.org/10.1007/s10854-015-4200-z
7. A. Ali, M. Z. Hira Zafar, I. ul Haq, A.R. Phull, J.S. Ali, A. Hussain, Synthesis, characterization, applications, and challenges of iron oxide nanoparticles. Nanotechnol Sci Appl, 9 (2016) 49. https://www.ncbi.nlm.nih.gov/pmc/articles/PMC4998023/
8. Alibeigi S, Vaezi M (2018) Phase transformation of iron oxide nanoparticles by varying the molar ratio of Fe^{2+}:Fe^{3+}. Chem Eng Techno 47:777–780. https://doi.org/10.1002/ceat.200800093
9. Bhavani P, Reddy N, Reddy I, Sakar M (2017) Manipulation over phase transformation in iron oxide nanoparticles via calcination temperature and their effect on magnetic and dielectric properties. IEEE Trans Magn 9:1–5. https://doi.org/10.1109/TMAG.2017.2715320

10. Hu Y, Kleiman-Shwarsctein A, Forman A, Hazen D, Park J, McFarland E (2008) Pt-doped α-Fe_2O_3 thin films active for photoelectrochemical water splitting. Chem Mater 20:3803–3805. https://doi.org/10.1021/cm800144q
11. Kleiman-Shwarsctein A, Hu Y, Forman A, Stucky G, McFarland E (2008) Electrodeposition of α-Fe_2O_3 doped with Mo or Cr as photoanodes for photocatalytic water splitting. J Phys Chem C 112:15900–15907. https://doi.org/10.1021/jp803775j
12. Xiao Z, Li J, Zhong J, Hu W, Zeng J, Huang S, Li M (2014) Enhanced photocatalytic decolorization of methyl orange by gallium-doped α-Fe_2O_3. Mater Sci Semicond Process 24:104–109. https://doi.org/10.1016/j.mssp.2014.03.028
13. Guo L, Chen F, Fan X, Cai W, Zhang J (2010) S-doped α-Fe_2O_3 as a highly active heterogeneous Fenton-like catalyst towards the degradation of acid orange 7 and phenol. Appl Catal B 96:162–168. https://doi.org/10.1016/j.apcatb.2010.02.015
14. Wei Y, Han S, Walker D, Warren S, Grzybowski B (2012) Enhanced photocatalytic activity of hybrid Fe_2O_3–Pd nanoparticulate catalysts. Chem Sci 3:1090–1094. https://doi.org/10.1039/C2SC00673A
15. Tang H, Yin W, Matin M, Wang H, Deutsch T, Al-Jassim M, Yan Y (2012) Titanium and magnesium Co-alloyed hematite thin films for photoelectrochemical water splitting. J Appl Phys 111:073502. https://doi.org/10.1063/1.3699016
16. Thimsen E, Formal F, Grätzel M, Warren S (2011) Influence of plasmonic Au nanoparticles on the photo activity of Fe_2O_3 electrodes for water splitting. Nano Lett 11:35–43. https://doi.org/10.1021/nl1022354
17. Jang J, Yoon K, Xiao X, Fan F, Bard A (2009) Development of a potential Fe_2O_3-based photocatalyst thin film for water oxidation by scanning electrochemical microscopy: effects of Ag–Fe_2O_3 nanocomposite and Sn doping. Chem Mater 21:4803–4810. https://doi.org/10.1021/cm901056c
18. Deshmane V, Patil A (2019) Synergy of semiconductor (Hematite) & catalytic (Ni) properties enhance gas sensing behavior to NO_2. Mater Res Express 6:075910. https://doi.org/10.1088/2053-1591/ab165e
19. Deshmane V, Patil A (2019) Study of In_2O_3& α-Fe_2O_3 nano-composite as a petrol vapor sensor. Mater. Res. Express 6:025904. https://doi.org/10.1088/2053-1591/aaed90/meta
20. Ristić M, Popović S, Tonković M, Music S (1991) Chemical and structural properties of the system Fe_2O_3-In_2O_3. J Mater Sci 26:4225–4233. https://doi.org/10.1007/BF02402973
21. Pandey B, Shahi A, Shah J, Kotnala R, Gopal R (2013) Optical and magnetic properties of Fe_2O_3 nanoparticles synthesized by laser ablation/fragmentation technique in different liquid media. Appl Surf Sci 289(289):462–471. https://doi.org/10.1016/j.apsusc.2013.11.009
22. Singh R, Koli P, Jagdale B, Patil A (2019) Effect of firing temperature on structural and electrical parameters of synthesized CeO2 thick films. SN App Sci. https://doi.org/10.1007/s42452-019-0246-5
23. Shinde R, Khairnar S, Patil M, Adole V, Koli P, Deshmane V, Halwar D, Shinde R, Pawar T, Jagdale B, Patil A (2022) Synthesis and characterization of ZnO/CuO nanocomposites as an effective photocatalyst and gas sensor for environmental remediation. J Inorg Organomet Polym Mater 32:1045–1066. https://doi.org/10.1007/s10904-021-02178-9
24. Mizsei J (2016) Forty Years of Adventure with Semiconductor Gas Sensors. Procedia Eng 168:221–226. https://doi.org/10.1016/j.proeng.2016.11.167
25. M. Ivanovskaya, Ceramic and film metal oxide sensors obtained by sol-gel method: structural features and gas-sensitive properties, Electron Technol. 33 (2000) 108–112. https://www.infona.pl/resource/bwmeta1.element.baztech-article-BWA1-0001-0917
26. Garje A, Sadakale S (2013) LPG sensing properties of platinum dopes nano-crystalline SnO_2 based thick films with the effect of dipping time and sintering temperature. Adv Mater Lett 4910:58–63
27. Windischmann H (1979) A model for the operation of a thin-film SnO x conductance-modulation carbon monoxide sensor. J Electrochem. Soc. 126:627. https://doi.org/10.1149/1.2129098/meta
28. Sorescu M, Xu T, Diamandescu L, Hileman D (2011) Synthesis and characterization of indium oxide-hematite magnetic ceramic solid solution. Hyperfine Interact 199:365–386. https://doi.org/10.1007/s10751-011-0267-y
29. Morganti KJ, Foong TM, Brear MJ, da Silva G, Yang Y, Dryer FL (2013) The research and motor octane numbers of liquefied petroleum gas (LPG). Fuel 108(2013):797–811. https://doi.org/10.1016/j.fuel.2013.01.072
30. Deshmane V, Patil A (2020) Cobalt oxide doped hematite as petrol vapor sensor. Mater Chem Phys 246:122813. https://doi.org/10.1016/j.matchemphys.2020.122813
31. Tang H, Yan M, Zhang H, Li S, Ma X, Wang M, Yang D (2006) A selective NH_3 gas sensor based on Fe_2O_3–ZnO nanocomposites at room temperature. Sens Actuators B Chem 114:910–915. https://doi.org/10.1016/j.snb.2005.08.010
32. Hjiri M (2020) Highly sensitive NO_2 gas sensor based on hematite nanoparticles synthesized by sol-gel technique. J Mater Sci Mater Elec. https://doi.org/10.1007/s10854-020-03069-4
33. Hao D, Jinliang M, Fang Y, Pingyi G, Xiao J (2019) Size and morphology dependent gas-sensing selectivity towards acetone vapor based on controlled hematite nano/microstructure (0D to 3D). J Solid State Chem. https://doi.org/10.1016/j.jssc.2019.04.025
34. Jadhav V, Patil S, Shinde D, Waghmare S, Zate M, Mane R, Sung-Hwan H (2013) Hematite nanostructures: Morphology-mediated liquefied petroleum gas sensors. Sens Actuators B: Chem 188:669–674. https://doi.org/10.1016/j.snb.2013.07.072
35. Garcia-Osorio D, Hidalgo-Falla P, Peres H, Gonçalves J, Araki K, Garcia-Segura S, Picasso G (2021) silver enhances hematite nanoparticles based ethanol sensor response and selectivity at room temperature. Sensors. https://doi.org/10.3390/s21020440
36. Chen H, Jin K, Wang P, Xu J, Han Y, Jin H, Jin D, Peng X, Hong B, Li J, Yang Y, Gong J, Ge H, Wang X (2018) Highly enhanced gas-sensing properties of indium-doped mesoporous hematite nanowires. J Phys Chem Solids 120:271–278. https://doi.org/10.1016/j.jpcs.2018.05.004
37. Kima D, Kimb T, Sohnb W, Suhb J, Shimc Y, Kwonb K, Hongb K, Choib S, Byund H, Leea J, Jang H (2018) Au decoration of vertical hematite nanotube arrays for further selective detection of acetone in exhaled breath. Sens Actuators B: Chem 274:587–594. https://doi.org/10.1016/j.snb.2018.07.159
38. Hu J, Xiong X, Guan W, Long H (2022) Urchin-like PdO–Fe_2O_3 heterojunctions for high-performance hydrogen sulfide gas sensors. Ceram Int 48–8:10562–10573. https://doi.org/10.1016/j.ceramint.2021.12.269
39. Zhuang Z, Zhang L, Huang C, Wang X, Guo H, Thomas T, Qu F, Wang P, Yang M (2022) A dimethyl disulfide gas sensor based on nanosized Pt-loaded tetrakaidecahedral α-Fe2O3 nanocrystals. Nanotechnology. https://doi.org/10.1088/1361-6528/ac614c
40. Thua N, Cuong N, Nguyena L, Khieub D, Namd P, Toane N, Hunge C, Hieu N (2017) Fe_2O_3 nanoporous network fabricated from Fe_3O_4/reduced graphene oxide for high-performance ethanol gas sensor. Sens Actuators B: Chem. https://doi.org/10.1016/j.snb.2017.09.154

Authors and Affiliations

Vikas V. Deshmane[1] · Sarika Shinde[2] · Dharma K. Halwar[3] · Gotan Jain[2] · Arun V. Patil[4]

✉ Arun V. Patil
aruptl@gmail.com

[1] Department of Physics, SICES Degree College, Ambarnath, Thane, Maharashtra, India

[2] KKHA Arts, SMGL Commerce and SPHJ Science College, Chandwad, Nashik, Maharashtra, India

[3] Thick and Thin-Film Laboratory, M.S.G. College, Malegaon, Nashik, Maharashtra, India

[4] Department of Physics, MGV's Arts, Science, and Commerce College, Manmad, Nashik, Maharashtra, India